Enthalpy modulation of a laminar pulsed nitrogen arc jet: time-resolved diagnostics and model

Vincent Rat, Joanna Krowka, Jean-François Coudert

Enthalpy modulation of a laminar pulsed nitrogen arc jet: time-resolved diagnostics and model

V Rat[1], J Krowka and J F Coudert

CNRS, University of Limoges, SPCTS UMR7315, European Ceramic Centre 12 rue Atlantis 87068 Limoges cedex, France

In most studies, plasma spraying of liquid feedstock for ceramic coating elaboration requires limiting the arc motion to obtain stable plasma and to favour homogeneous treatment of nanomaterials. In this chapter, an alternative approach is proposed and consists of using a pulsed arc jet modulating the specific enthalpy in time. The momentum and heat transfers can be controlled provided a synchronous injection of materials is associated with it. The rotational temperatures of the nitrogen arc jet are measured by means of time-resolved optical emission spectroscopy synchronized with the arc voltage. The enthalpy modulation ratio (h_{max}/h_{min}) is shown to be close to 2.68. A simplified model of the dynamics of heat transfers is used to interpret diagnostics and highlights a time delay between arc voltage and enthalpy at the nozzle exit due to the characteristic time of heat transfers and residence time of plasma.

Keywords: thermal plasma, electric arc, fluctuations, diagnostics

1. Introduction

Deposition processes of ceramic coatings with nanostructured architectures are intensively studied because of strong needs in many applications fields, such as thermal barrier coatings for the gas turbine industry, fuel cells, and wear-resistant or photocatalytic coatings. In industrial applications, such refractory materials are deposited by cost-effective plasma spraying techniques possessing the advantage of being able to treat material with high rates (>kg/h) in high enthalpy mediums ($>10\,MJ\,kg^{-1}$) [1]. Ceramic nanostructured coatings can now be achieved whether nanopowders are dispersed in suspensions or liquid solution precursors are injected into thermal plasmas, respectively, corresponding to suspension plasma spraying and solution precursor plasma spraying. These emerging processes must be distinguished from the conventional plasma spraying technology because the use of the liquid phase as a carrier medium for solid material and the size of injected materials compel the consideration of new issues. The fragmentation processes of droplets, which depend on liquid and plasma properties, are responsible for the history of heat and momentum transfers of in-flight solid nanoparticles [2–5]. Moreover, submicron solid particles have low thermal and dynamic inertia so that heat and momentum transfers between plasma and particles are dependent to a large extent on spatial and temporal variations of plasma properties. Considering a relevant association of a plasma torch with compatible injection technology is a key point for control of coating properties.

Electric arc fluctuations in direct current (dc) plasma torches have been studied for a few decades, highlighting several modes of instabilities [6–12]. They originate in intricate magneto-hydrodynamic forces applied to the electrical current paths of the arc column and of the arc attachment at the anode wall, resulting in non-uniform and time-dependent heating of plasma-forming gases. In particular, in plasma torches for coating deposition, the characteristic time of arc root motion is a few tens of microseconds and corresponds to an electrical breakdown across the cold boundary layer,

[1] Author to whom any correspondence should be addressed.

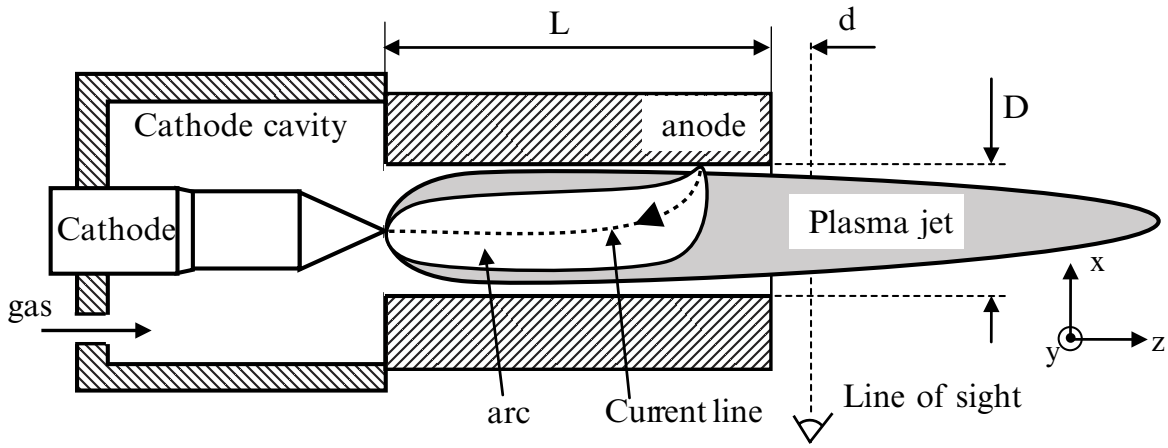

Figure 1. Simplified scheme of dc plasma torch.

giving rise to a new arc attachment upstream that reduces the arc voltage (restrike mode). This breakdown appears for low electric field values (~10^4 V m^{-1}) [12] because it is governed by a fast-developing overheating instability initiated by residual electrical conductivity around the arc column [13]. Larger instability time scales have also been observed (a few hundreds of microseconds) and are attributed to Helmholtz and acoustic oscillations [10, 14].

These arc instabilities obviously generate inhomogeneous and time-dependent plasma properties in arc jets that affect plasma transfers to materials. Important efforts are then devoted to improve the stability of torches either by means of acoustic effects in conventional torches (i.e. one cathode, one anode) [15] or by using complex multi-electrode torches [16]. In such systems, the amplitude of arc motion is reduced so that the arc voltage becomes only slightly time-dependent. In this chapter, an alternative approach using a strong fluctuating arc jet that can oscillate in a controlled manner is proposed [17]. It results in a successive emission of high and low plasma enthalpy regions at the nozzle exit. Because the vaporization time of droplets is inversely proportional to plasma enthalpy, the use of a pulsed injection system should permit control of plasma transfers by adjusting the injection timing that is characterized by a time delay, τ, in the following.

The purpose of this chapter is to show that the specific enthalpy is substantially modulated in a dc pulsed arc jet and to highlight the dynamics of arc voltage and enthalpy.

The next section presents the experimental set-up and procedures. Section 3 shows measurements of rotational temperatures obtained by time-resolved optical emission spectroscopy. The experimental results obtained are interpreted in the frame of local thermodynamic equilibrium, which is a classical assumption for plasma generated by electric arcs under atmospheric pressure [18]. A single temperature allows determining thermodynamic state functions and plasma chemical composition can be computed as a function of temperature and pressure by minimizing the Gibbs free energy.

Section 4 discusses the significance of measured temperatures to deduce the corresponding enthalpies. An analytical model associated with experimental measurements permits determination of the time-dependence relationship between arc voltage and enthalpy. Finally, the conclusion and perspectives are given.

2. Experimental descriptions and procedures

2.1. Self-sustained pulsed mode

Previous studies have shown that an arc confined within a plasma torch can oscillate following a self-sustained pulsed mode [12, 17]. It results from the resonant coupling of two modes of arc voltage fluctuations, namely the Helmholtz and restrike modes. The former mode is attributed to a reciprocal dependence of arc voltage and pressure inside the cathode cavity that contains the cold plasma-forming gas. When arc voltage varies due to plasma flow, pressure also changes what affects the mass flow rate, and in turn it modifies the plasma flow. The latter mode corresponds to an upstream re-arcing process that interrupts the arc elongation, i.e. the arc voltage, and causes a sudden voltage decrease. The voltage signal has a typical saw-tooth shape waveform of the restrike mode but it is driven by the Helmholtz resonance.

A homemade plasma torch operating at atmospheric pressure in ambient air is power-supplied by a current-regulated source. The arc burns between the thoriated tungsten cathode tip and a copper nozzle as seen in figure 1. Both electrodes are water-cooled by means of a single cooling water circuit. Upstream the gas feeding line, the mean gas flow rate is maintained constant during experiments and is controlled by a mass flowmeter permitting delivery of the nitrogen gas through the cathode cavity with flow rates ranging between 2 and 4 standard litres per minute (slm). The internal diameter of the nozzle channel, D, can be changed between 3 and 4 mm. The arc current I, the mean arc voltage $\bar{V}$, and the heat losses to the electrodes Q_{loss} are measured over a period of a few minutes. The values are used to determine the effective specific enthalpy, $\bar{h}_{\text{L}}$, available at the exit of the nozzle, L in length, such as $\bar{h}_{\text{L}} = (\bar{V}I - Q_{\text{loss}})/q_{\text{m}}$ where q_{m} is the gas mass flow rate. $\bar{h}_{\text{L}}$ represents a quantity that is averaged in time and also in the cross-section of the plasma jet at the torch exit. The heat losses to electrodes are evaluated by means of calorimetric measurements of torch cooling water.

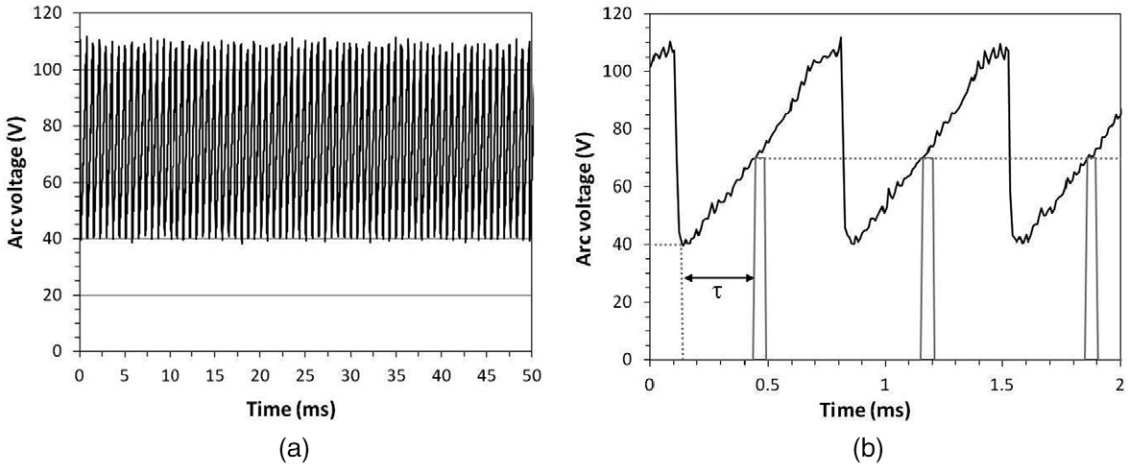

Figure 2. (a) Arc voltage signal of pulsed mode and (b) zoom of figure (a). A rectangular trigger signal in grey is added. The pulses are delayed by τ after voltage falling front and are used for triggering time-resolved diagnostics or injection of materials into the arc jet. Experimental parameters: $I = 15\,\text{A}$, $q_m = 4.510^{-5}\,\text{kg s}^{-1}$, and $D = 4\,\text{mm}$.

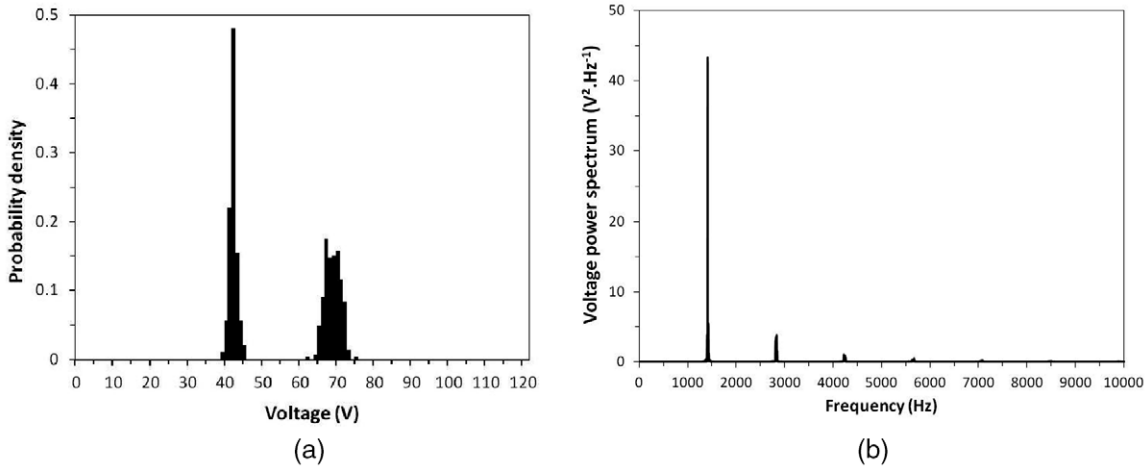

Figure 3. (a) Probability density of voltage minima (mean minimum voltage $\bar{V}_{min} = 40.96$ V) and amplitudes (mean amplitude $\bar{A} = 67.69$ V) in the signal of figure 1(a). (b) Power spectrum of arc voltage of figure 1(a).

This set of measurements is also used to check the reproducibility of results. The instantaneous arc voltage, $V(t)$ where t is time, is measured by using a data acquisition computer card piloted by Labview software at a sampling rate of $320\,\text{kS s}^{-1}$ during 0.2 s, giving a maximum frequency of 160 kHz and a frequency resolution of 5 Hz in calculated power spectra.

Figures 2(a) and (b) depict the voltage signal obtained with a pure nitrogen arc jet plasma (arc current $I = 15\,\text{A}$, nitrogen flow rate 2.1 slm or $4.5\ 10^{-5}\,\text{kg s}^{-1}$). The mean arc voltage is $\bar{V} = 73.7$ V and the mean specific enthalpy $\bar{h}_L = 13.4 \pm 1\,\text{MJ kg}^{-1}$. During the lengthening phase of the arc, the voltage increases from its minimum value, i.e. from 40 V up to 110 V. Then, because of the rearcing process, the voltage decreases to 40 V within less than 30 μs. It has been observed that the pulsed mode is quite stable over a few tens of minutes.

Figure 3(a) shows the probability density of the voltage minima and amplitudes of signal in figure 2(a). It corresponds to results obtained with 285 samples, i.e. from a voltage signal sampled during 0.2 s. The mean minimum voltage is $\bar{V}_{min} = 40.96$ V corresponding to a standard deviation of 1.05 V, and the mean amplitude is $\bar{A} = 67.69$ V corresponding to a standard deviation of 2.10 V. Due to the triangular shape of the periodic voltage, the values of $\bar{V}$ and of $\bar{V}_{min} + \bar{A}/2$ are comparable even though they are measured independently and over different time scales. Finally, figure 3(b) displays the power spectrum of arc voltage in figure 2(a) and exhibits a strong fundamental frequency at approximately 1410 Hz and its higher frequencies harmonics.

2.2. Time-resolved diagnostics

Figure 4 presents the experimental set-up consisting of a dc plasma torch, a fast-shutter camera, a spectrometer, and a synchronization unit. Time-resolved imaging of plasma jet is performed by means of a fast-shutter camera (PCO, Kelheim, Germany) with high resolution (1392 × 1040 pixels) and that can be externally triggered.

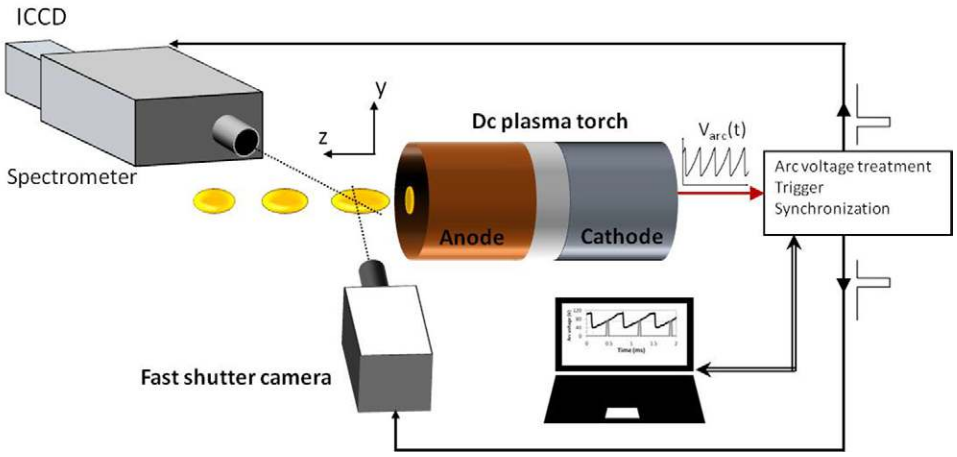

Figure 4. Experimental set-up.

Optical emission spectroscopy (OES) is performed by using the IsoPlane spectrograph (Princeton Instruments, Trenton, NJ, USA). The focal length is 320 mm and the focal plane size is 27 mm wide × 14 mm high. The arrangement of optical components reduces optical aberrations that ensure a constant spectral resolution at each point of the focal plane. The spectrograph is equipped with a triple grating turret (68 mm × 68 mm grating size). It is associated with an Intensified CCD camera (PIMAX4 1024i, Princeton Instruments, Trenton, NJ, USA) with high resolution (1024 × 1024 pixels, 12.6 μm pixel size) including a fast gate intensifier (down to 3 ns). A UV objective (105 mm focal length, f/4 aperture ratio) is mounted on the spectrograph to image the plasma, providing −0.3 magnification. Lightfield software (64 bits, Princeton Instruments, Trenton, NJ, USA) is used to control spectroscopic devices and to record the spectra.

The spectrometer is calibrated by means of a tungsten ribbon lamp used as a standard source that is power-supplied by a current-regulated source. A pyrometer is used to measure the tungsten ribbon temperature at a given lamp current. The spectral radiance of the tungsten ribbon lamp is calculated for a given temperature by using Planck's law and the spectral emissivity of tungsten given by De Vos [19]. The spectrometer response to the tungsten ribbon lamp is known for a given set of spectrometer parameters that enables deducing the spectral radiance of the plasma. The linear response of the ICCD detector to spectrometer parameters has been checked.

The falling fronts of the voltage signal represent rather accurate events that are used to define rectangular pulses (figure 2(b)), delayed by an adjustable amount of time, τ, and ranging between 0 and 800 μs. Because of a synchronization device, these pulses are used to trigger both the fast-shutter PCO camera and the ICCD detector, so that the plasma pictures and the spectrum are simultaneously recorded for a given instantaneous voltage (for example: $\tau = 300\,\mu$s, 70 V in figure 2(b)). The exposure time of the camera is $\tau_{exp} = 30\,\mu$s and the rate is limited to 12 frames per second. For the ICCD, the exposure time, τ_{gate}, is between 15 and 30 μs for each received trigger. It is possible to accumulate N_{acc} signals at a rate corresponding to the pulsed mode frequency that is 1410 Hz, so that the total exposure time is $N_{acc}.\tau_{gate}$. The number N_{acc} is between 10 and 500, depending on operating conditions.

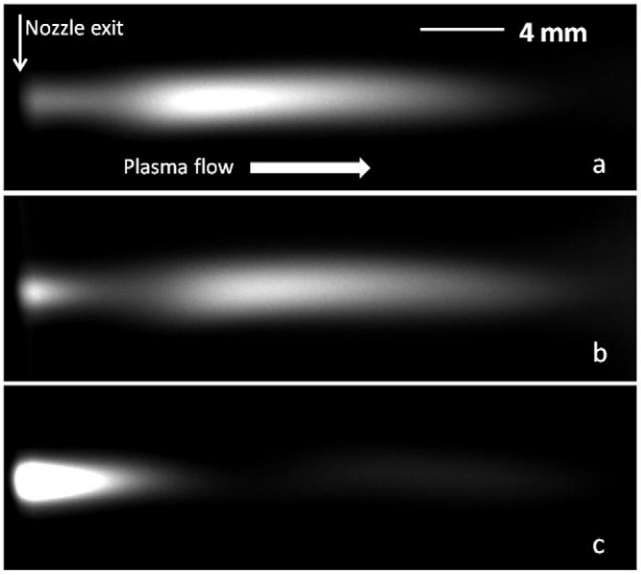

Figure 5. Pictures of the N_2 arc jet working in pulsed mode. The PCO camera is triggered after different time delays and the time aperture is 30 μs. (a) $\tau = 140\,\mu$s. (b) 220 μs. (c) 340 μs. During the time aperture, the torch voltage increases by 3 V.

Figure 5 displays time-resolved imaging of the pulsed arc jet triggered for three different delays: τ = 140, 220, and 340 μs. Due to the time aperture of 30 μs, the torch voltage corresponds to the intervals 54–57 V, 62–65 V, and 74–77 V for figures 5(a)–(c), respectively. These pictures are taken for the same experimental conditions as those of figure 2, and the operating parameters for the image captures are the same for the three figures. For higher voltages, this requires the use of a neutral filter so that the pictures are not easily comparable and are not shown here. Both specific enthalpy and emission of radiation are monotonous increasing functions of temperature so that the effective emission coefficient of the plasma is an increasing function of specific enthalpy [18]. In figure 5(a) the high enthalpy region can be seen at approximately 8 mm from the nozzle exit, which corresponds to the convection of high plasma energy density, generated in the preceding period. In

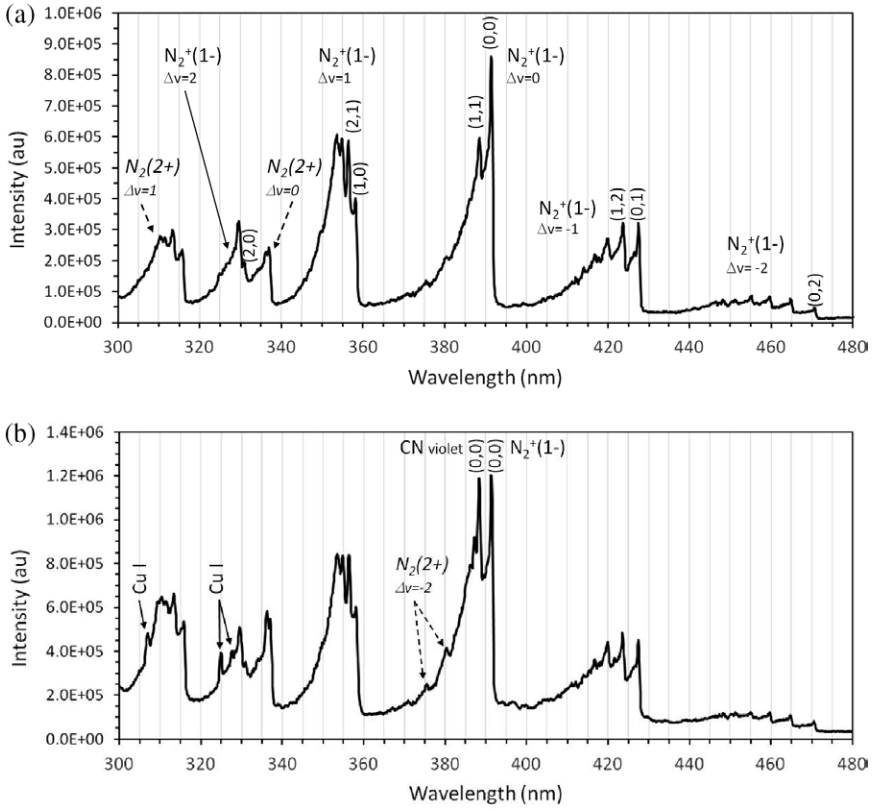

Figure 6. Time-averaged spectra of pulsed arc jet recorded for two distances from the nozzle exit: (a) $d = 1$ mm and (b) $d = 6$ mm. Exposure time 7 ms corresponding to 10 periods in figure 2.

figure 5(b), this hot plasma region is recombining due to the surrounding air cooling whereas a new arc jet is being formed at the nozzle exit. In figure 5(c), close to the nozzle exit, the new arc jet has increased energy density while the preceding plasma region has almost extinguished.

These pictures demonstrate qualitatively that the plasma flow properties are time-modulated and space-modulated. Going further in the diagnostic requires quantitative measurement that can be provided by emission spectroscopy techniques. Because of the use of nitrogen as the plasma gas, the analysis of molecular bands is chosen to determine the rotational temperature as a function of the instantaneous voltage and as a function of the distance from the nozzle exit.

3. Time-resolved measurements of rotational temperature

3.1. Identification of emitting molecular systems

The objective of this section is to describe the emitting diatomic molecular systems to isolate the relevant parts of the spectrum used in molecular simulation for rotational temperature measurement. The spectra are recorded between 300 nm and 480 nm at low spectral resolution ($\Delta\lambda = 2.946$ nm) with an exposure time of the ICCD detector of approximately 7 ms, i.e. approximately 10 periods of arc voltage signal (figure 2). For that part, the synchronization device is not used.

Figures 6(a) and (b) depict typical molecular spectra recorded at $d = 1$ mm and $d = 6$ mm, respectively, from the nozzle of the plasma torch.

Following the notations used in spectroscopy, the total energy of a diatomic molecule, T in cm^{-1}, is given by:

$$T = T_e + G(v) + F_v(J) \quad (1)$$

where T_e is the electronic spectral term, $G(v)$ is the vibrational spectral term, v is the vibrational quantum number, $F_v(J)$ is the rotational spectral term, and J is the rotational quantum number.

The vibrational term is given by:

$$G(v) = \left(v + \frac{1}{2}\right)\omega_e - \left(v + \frac{1}{2}\right)^2 \omega_e x_e + \left(v + \frac{1}{2}\right)^3 \omega_e y_e + \ldots \quad (2)$$

where ω_e, $\omega_e x_e$, and $\omega_e y_e$ are spectroscopic constants for a given electronic state [20].

As expected, the emission of the first negative system of the molecular ion N_2^+, $N_2^+(1-)$, is mainly observed. It corresponds to the transition between the $B^2\sum_u^+$ state at 18.7 eV and the $X^2\sum_g^+$ state at 15.6 eV [21–23]. This transition between both $^2\sum^+$ states ($\Lambda = 0$) corresponds to a pure case b of Hund. Only transitions $\Delta K = -1$ and $\Delta K = 1$ are allowed, where K is the rotational quantum number, resulting in only P and R branches in the spectrum. Each rotational state is spin-doubled such as $J = K + 1/2$ and $J = K - 1/2$ due to spin multiplicity ($2S + 1 = 2$).

Spectroscopic data together with equations (1) and (2) allow identification of the different vibrational sequences ($\Delta v = v' - v''$) of $N_2^+(1-)$, which are indexed in figure 6(a). The single prime corresponds to an upper vibrational level and the double prime corresponds to a lower level. The main head

bands of different vibrational bands (v',v'') are also reported in figure 6(a). We observe the $\Delta v = -2,\ -1,\ 0\ ,\ 1\ ,$ and 2 vibrational sequences of $N_2^+(1-)$. The most prominent vibrational sequence corresponds to $\Delta v = 0$, with the head bands (0,0) and (1,1), respectively, at 391.4 nm and 388.4 nm.

The second positive system of the molecule N_2, $N_2(2+)$, is also observed. This system corresponds to the transition between the state $C\,^3\Pi_u^+$ at 11.1 eV and the state $B\,^3\Pi_g^+$ at 7.39 eV. The rotational structure is by far more complicated than $N_2^+(1-)$ because the coupling follows Hund's case a for low J rotational numbers ($J < 15$) and Hund's case b for higher values. According to the measured spectrum in figure 6(a), $\Delta v = 0$ and $\Delta v = 1$ vibrational sequences are mainly observed in the spectrum.

Very close to the nozzle exit, the emitting systems correspond to species coming from the plasma-forming gas, i.e. N_2, N_2^+, but also atomic nitrogen NI (triplet between 742 and 747 nm, not shown in figure 6(a)). However, as shown in figure 6(b), the emitted radiation is evidently related to the distance from the nozzle exit because of plasma mixing with the ambient atmosphere. Figure 6(b) depicts a measured spectrum obtained in the same conditions as that of figure 6(a) but recorded at 6 mm from the nozzle exit. It can be mainly seen that the $\Delta v = 0$ vibrational sequence of $N_2^+(1-)$ system is altered. The CN violet system, due to the formation of CN molecule coming from the carbon dioxide in air, is similar to that of $N_2^+(1-)$ and corresponds to transition between the $B\,^2\Sigma^+$ state at 3.32 eV to the ground state $X\,^2\Sigma^+$. It also follows the coupling of Hund's case b. The $(0-0)$ head band is approximately 388.3 nm and overlaps the $(1-1)$ head band of the first negative system of N_2^+ [20]. Moreover, it can be noted that the $\Delta v = -2$ sequence of the second positive system of N_2 also overlaps $N_2^+(1-)$ at approximately 380 nm. Finally, atomic copper lines of Cu I corresponding to 306.341, 324.754, and 327.396 nm are observed and are obviously due to anode erosion because of the arc attachment at the anode wall.

Preliminary tests have shown that choosing the $N_2(2+)$ instead of the $N_2^+(1-)$ system gives rise to an increase of uncertainty, however, with compatible values of rotational temperature. This poor precision is due to the overlapping of bands at high temperature.

For accuracy reasons, in the following the rotational temperature is measured from the $\Delta v = 0$ vibrational sequence of the $N_2^+(1-)$ system, i.e. between 363 and 392 nm. Spectra are measured at different distances from the nozzle exit and for different time delays τ or related trigger voltages. For high trigger voltages, the overlapping of the $\Delta v = -2$ sequence of the second positive system of N_2 is weak at weak distances from the nozzle exit ($\leqslant$6 mm) and is neglected for temperature measurements. For the same reason, the overlapping of the CN violet system with the (1,1) band of $N_2^+(1-)$ can also be neglected.

3.2. Principle of measurements of rotational temperature

The radiative intensity is recorded following side-on observation, that is to say, the emission coefficient, $\varepsilon_\lambda(x, y)$, is integrated along the line of sight (x direction) for each wavelength. In addition, the binning procedure is used, i.e. it consists of summing the recorded values in the height direction (y) so that the cross-section of the plasma jet located at distance z from the nozzle exit is assimilated to a point source. No Abel's inversion is performed and no information is available concerning the local values of the emission coefficient.

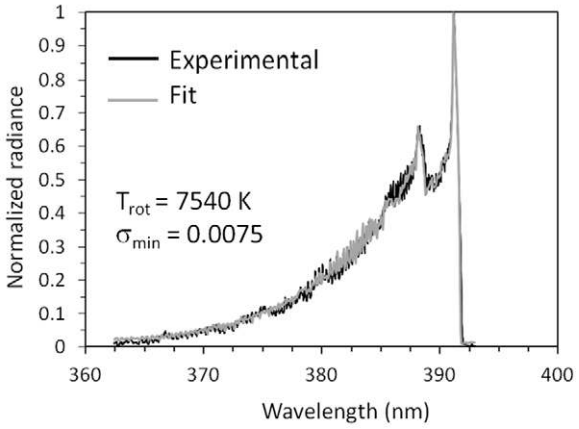

Figure 7. Experimental normalized spectral of $N_2^+(1-)$ system and its numerical fit obtained by Specair (T_{rot}: rotational temperature, σ_{min}: residual).

Rotational temperatures are measured by means of spectral simulation of the $N_2^+(1-)$ system using Specair software [24] between 363 and 392 nm at low spectral resolution. Specair is a commercial software used to simulate radiative molecular and atomic transitions in air plasma, including $N_2(2+)$, $N_2^+(1-)$, and CN violet systems. Specair assumes a Boltzmann distribution of rotational states at the rotational temperature T_{rot}, which is supposed to be close to the gas temperature in our experimental conditions [25]. It permits simulation of the absolute intensities of radiative transitions for a given slit function and allows spectral fit of the experimental spectra to be obtained.

The Specair spectral simulation and the spectral fit procedure to obtain the optimized rotational temperature require subtracting background radiation before calibration. Finally, the slit function data are input in Specair and are determined by the use of a mercury standard lamp.

Figure 7 depicts an experimental spectrum of $N_2^+(1-)(\Delta v = 0$ sequence), obtained for a trigger voltage of 105 V at $d = 1$ mm from the nozzle exit and its numerical simulation that is fitted to experimental values. Let σ be the root-mean square between the experimental spectral profile and the theoretical profile simulated for a given rotational temperature T. The function $\sigma(T)$ presents a more or less sharp minimum so that for the best fit, $\sigma = \sigma_{min}$ and $T = T_{rot}$. In the minimum vicinity, σ can be expanded following $\sigma = \sigma_{min} + {}^1\!/_2 a(T - T_{rot})^2$, where a is the curvature of the $\sigma(T)$ function that is discretely evaluated with a set of guessed T values. Thus, the uncertainty δT is defined so that $\sigma(T_{rot} \pm \delta T) = 2\sigma_{min}$ that yields $\delta T = \sqrt{{}^{2\sigma_{min}}\!/_a}$. For a perfect fit, $\sigma_{min} = 0$ and $\delta T = 0$ and for $\sigma_{min} \neq 0$, δT decreases if the curvature is more pronounced.

In the following, the residuals of rotation temperature measurements obtained with Boltzmann distributions are

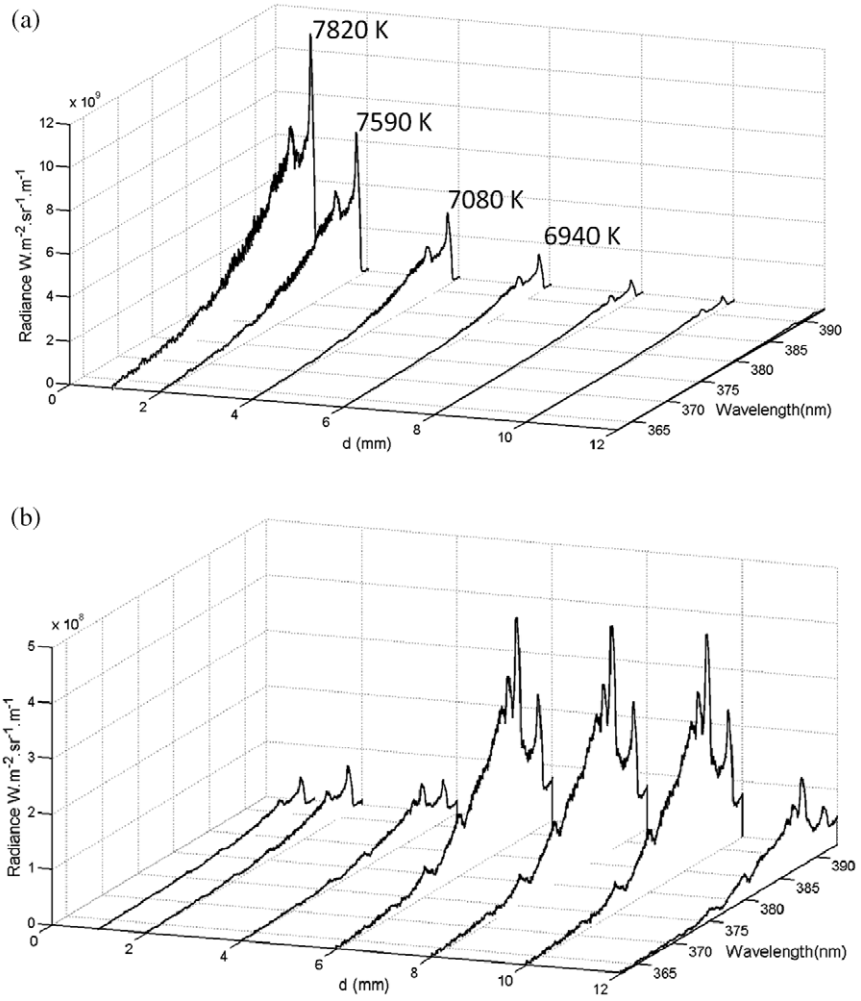

Figure 8. Measured emission spectra of pulsed N_2 arc jet for different distances d from nozzle exit and for two trigger voltages (a) $\tau = 700\,\mu$s and 110 V (rotational temperatures deduced from the best-fit Specair spectra are indicated) and (b) 140 μs and 54 V (figure 2).

less than 10^{-2}. By using the synchronization procedure and provided the resonant mode of the torch is locked, the spectrometer measurements give very reproducible measurements. A sensitivity analysis, which depends on input parameters as the slit function or a wavelength adjustment, shows a rotational temperature uncertainty δT less than 150 K in the case of figure 7. This low value of δT also indicates that T_{rot} is measured in a region where the temperature profile presents a rather flat maximum.

3.3. Influence of distances from the nozzle exit and trigger voltages on rotational temperatures

Figure 8(a) portrays the absolute intensities of $N_2^+(1-)$ spectra measured between 1 and 10 mm from the nozzle exit gated at maximum voltage ($\tau = 700\,\mu$s −110 V; figure 2). Rotational temperatures obtained from the best-fit Specair spectra are also indicated. This trigger voltage corresponds to the case where the arc length is a maximum, i.e. the highest specific enthalpy. The emitting plasma volume is the largest so that the number of emitting molecular ions is also a maximum. At 1 mm from the nozzle exit, the intensity is highest as is the rotational temperature, specifically 7820 K.

When the distance from the nozzle exit increases, the intensities decrease because of plasma cooling. Rotational temperatures decrease to 6940 K at 6 mm from the nozzle exit. At distances higher than 6 mm, the fitting procedure gives rise to unreliable rotational temperatures with residual higher than 10^{-2}.

Figure 8(b) shows the absolute intensities of $N_2^+(1-)$ spectra measured between $d = 1$ and 10 mm from the nozzle exit gated at a trigger voltage of 54 V (figure 5(a)). It is interesting to note that the absolute intensities of spectra are weak between 0 and 4 mm, but they start increasing at higher distances between 6 and 10 mm, and then decrease again at 12 mm as suggested in figure 5(a). Actually, the spectra are much more complicated than those obtained at 110 V because they include the overlapping of $N_2^+(1-)$, $N_2(2+)$ and CN violet systems.

The CN violet system gives the most prominent contribution at approximately 388 nm because of carbon dioxide contained in air that reacts with the nitrogen plasma. However, note that at only 1 mm from the nozzle exit, the spectra is dominated by the $N_2^+(1-)$ system. Rotational temperatures are not measured due to high residuals when fitting.

Consequently, the influence of trigger voltages on rotational temperatures can be determined with reliability for relatively high trigger voltages and close to the nozzle exit.

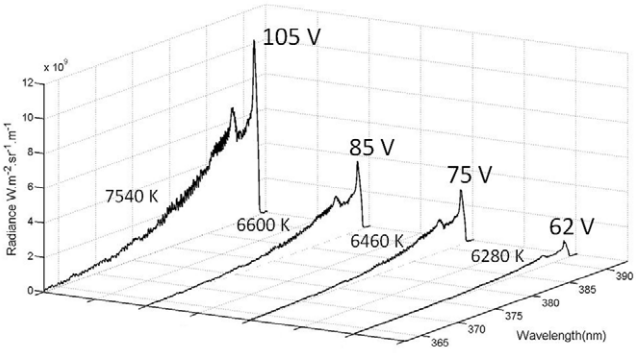

Figure 9. Measured emission spectra of pulsed N_2 arc jet at d = 1 mm from nozzle exit for different instantaneous voltages (105 V, 85 V, 75 V, and 62 V, ± 1.5 V). The rotational temperatures are deduced from the best-fit Specair spectra.

Figure 9 depicts the absolute intensity of the $N_2^+(1-)$ spectra measured at 1 mm from the nozzle exit for different trigger voltages, namely 105, 85, 75, and 62 V.

Reliable rotational temperatures were not obtained for voltages lower than 62 V. In this range of trigger voltage, the rotational temperatures vary between 6280 ± 250 K and 7540 ± 150 K.

In the next section, a discussion is provided about the relationships between the measured temperatures and the enthalpy available in the plasma jet for material processing.

4. Discussion

4.1. Temperature measurements

One of main issue of this chapter is determining whether the modulation of specific enthalpy in such pulsed plasma is of interest for material processing. First, it is important to evaluate the amplitude of modulation thanks to previous spectroscopic measurements. Second, the dynamic relationship between the arc voltage and the specific enthalpy must be discussed because the time delay τ is the key experimental parameter used to trigger the material injection within plasma for ceramic deposition [12, 17].

Figure 10 is the specific enthalpy of N_2 plasma calculated between 2000 and 12 000 K at atmospheric pressure under the local thermodynamic equilibrium assumption [26].

The steep slope between 6000 and 8000 K mainly corresponds to the dissociation of nitrogen molecules. In this temperature range, the N atoms concentration varies between from 2.5 10^{23} and 8.1 10^{23} m^{-3}. This also means that the increase of thermal energy is accompanied by important chemical energy storage.

The dashed lines represent the range of temperature measurements obtained in OES experiments, namely between 6280 K and 7820 K.

Figure 10 shows that the specific enthalpy should be modulated between 14.35 and 38.20 MJ kg^{-1}, i.e. a modulation ratio of 2.66. However, note that the mean specific enthalpy $\bar{h}_L$ determined in section 2.1 by measuring the electrode heat losses Q_{loss} and the mean arc voltage ($\bar{V}$ = 73.7 V), $\bar{h}_L$

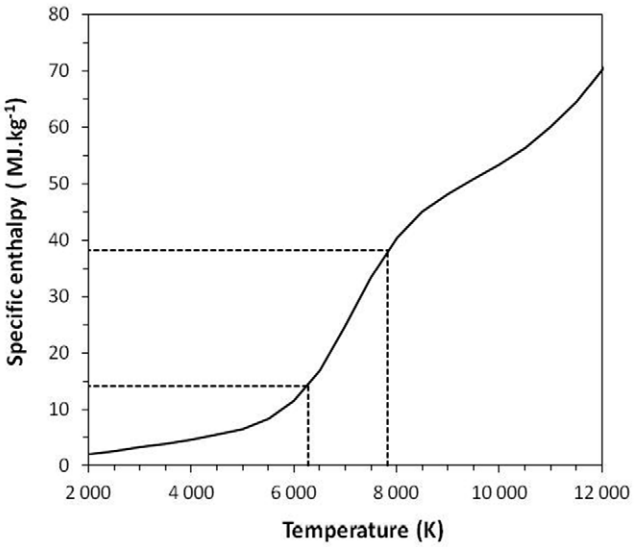

Figure 10. Specific enthalpy of N_2 plasma at local thermodynamic equilibrium and atmospheric pressure. Dashed lines show the range of temperatures measured by OES.

= 13.4 MJ kg^{-1} is smaller than 14.35 MJ kg^{-1}, which was obtained when triggering at 62 V. This difference cannot only be attributed to measurement precision, although in this temperature range only 100 K variation entails more than a 1 MJ kg^{-1} change in enthalpy. Measurements of plasma temperature result from measurements integrated along the line of sight and from the binning process of the height of plasma jet. They are not strictly speaking about mean temperatures, but they encompass the contributions of the plasma regions with different temperatures. As mentioned, the Abel's inversion was not performed. This is a deliberate choice, because this requires several hundreds of inversions for a single spectrum that provokes noise amplification and significantly increases the residual obtained at the end of the fitting procedure. The measured temperature, T_{rot}, is a weighted mean value of the temperatures related to the most luminous regions that are observed [27]. To improve the precision and also the interpretation of these measurements, the relationship between the measured temperature and the specific enthalpy, averaged in an arc jet cross-section, is investigated as follows. At time t, it is assumed that, at the nozzle exit, the specific enthalpy profile $h(r)$ is parabolic, because of the laminar feature of the plasma flow as shown [12, 17]:

$$h(r) = h_w + 2(h_L - h_w)\left(1 - \left(\frac{2r}{D}\right)^2\right) \quad (3)$$

where h_w and h_L, respectively, are the enthalpy at the anode wall and the enthalpy averaged over the arc jet cross-section, i.e. $h_L = \frac{1}{R^2}\int_0^R 2rh(r)\mathrm{d}r$ with $R = D/2$. h_L is time-dependent, with a mean value referred to as $\bar{h}_L$. For a wall temperature of approximately 500 K, $h_w \sim 0.2$ MJ kg^{-1} so that $h_w \ll h_L$. Following thermodynamic data, such as those of figure 10, a temperature profile, T(r), is determined that shows a rather flat maximum due to the steep slope of the $h(T)$ function between 6000 and 9000 K. Then, the emission coefficient

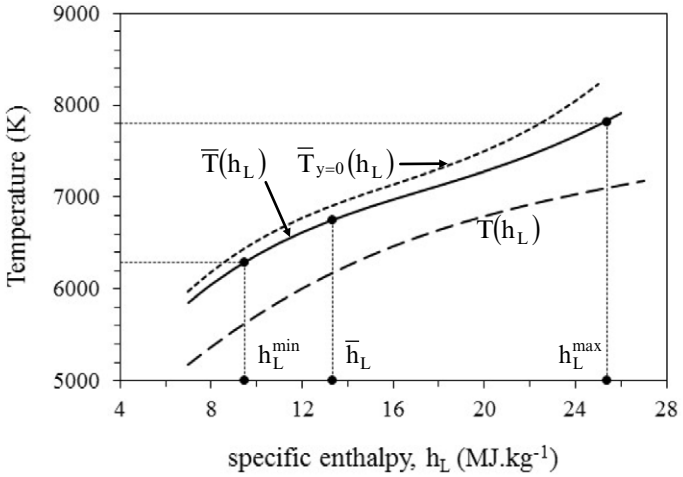

Figure 11. Dependence on specific enthalpy of the weighted temperatures $\bar{T}(h_L)$ and $\bar{T}_{y=0}$. The T(h_L) curve, which is the reciprocal of that of figure 10, is plotted for comparison.

$\varepsilon_{N_2^+}$ of the $N_2^+(1-)$ $\Delta v = 0$ sequence is computed as a function of $T(r)$, assuming local thermodynamic equilibrium. The emission coefficient increases monotonously almost by three decades when temperature varies from 5000 to 9000 K. This last temperature appears to be a maximum in the present experimental conditions because it corresponds to a specific enthalpy of 48 MJ kg^{-1} (figure 10), which cannot be reached.

The weighted mean value of the plasma temperature at the nozzle exit is then calculated as a function of h_L, following:

$$\bar{T}(h_L) = \frac{\int \varepsilon_{N_2^+}(r) T(r) r \mathrm{d}r}{\int \varepsilon_{N_2^+}(r) r \mathrm{d}r} \qquad (4)$$

where the integration is performed over the entire cross-section of the jet.

If the integration is only performed along the line of sight crossing the jet axis at $y = 0$, then the weighted temperature $\bar{T}_{y=0}$ is obtained as a function of h_L. Because the emission coefficient presents a sharp maximum at the jet axis, $\bar{T}_{y=0}$ is only slightly lower than the maximum temperature, T_{max}, and $\bar{T}(h_L) < \bar{T}_{y=0}(h_L) < T_{max}$.

Figure 11 shows the dependence of $\bar{T}(h_L)$ and $\bar{T}_{y=0}(h_L)$ on the space-averaged specific enthalpy. The temperature $T(h_L)$, defined as the reciprocal function of that plotted in figure 10, has been added. The significant difference that can be observed in figure 11 between $\bar{T}(h_L)$ and $T(h_L)$ is due to the fact that these temperatures are averaged over a cross-section with non-linear and very different weight functions, namely $\varepsilon_{N_2^+}(T)$ and $h(T)$, respectively.

It is then assumed that T_{rot} is corresponding to a $\bar{T}(h_L)$ value within the interval $\pm \delta T$. The $\bar{T}(h_L)$ curve in figure 11 is used to convert the measured temperatures reported in figure 9 into specific enthalpies. At the nozzle exit, the reliable temperatures range between 6280 ± 250 K (figure 9) and 7820 ± 150 K (figure 8(a)) corresponding to the respective voltages 62 and 110 V, to $h_L^{min} = 9.5 \pm 1.5$ MJ kg^{-1}, and to $h_L^{max} = 25.5 \pm 1.5$ MJ kg^{-1} instead of 14.35 and 38.20 obtained previously. In addition, the time and space-averaged value measured calorimetrically, $\bar{h}_L = 13.4$ MJ kg^{-1}, is now lying between h_L^{min} and h_L^{max}. Note that the modulation ratio of enthalpy remains close to the previous one, i.e. 2.68.

In previous work [12, 17], it was assumed that the heat losses are constant so that an equivalent constant voltage can be defined as $V_{loss} = Q_{loss}/I$ with a measured value $V_{loss} = 36$ V. If the relationship $\bar{h}_L = (\bar{V}I - Q_{loss})/q_m$ that holds for the stationary state is still valid when considering the fluctuations, then $h_L(t) = (V(t) - V_{loss})I/q_m$ yields, for $40 < V(t) < 110$ V (figure 2), $1.5 < h_L(t) < 26$ MJ kg^{-1}. This range corresponds to a theoretical modulation ratio of 17 instead of 2.66 as found previously. If the 26 MJ kg^{-1} value is close to h_L^{max} that was deduced from the OES results (figure 11), then h_L^{min} is much higher than 1.5 MJ kg^{-1}, which also gives an overestimation of the modulation ratio. One possibility to explain this non-agreement is that OES cannot measure the temperature below a certain threshold as suggested above when the voltage is lower than 62 V. Another explanation, which does not exclude the previous one, is that the stationary heat balance cannot be transposed to the fluctuating behaviour of the arc jet. The following section is devoted to a more accurate insight of the transient phenomena involved in the energy balance of the plasma torch.

4.2. Evaluation of electrode heat losses at steady state

In the previous analysis, the heat losses are supposedly independent of the specific enthalpy, even though the plasma is contained in the water-cooled nozzle. Due to the single cooling circuit, the heat losses to electrodes include the anode and cathode contributions. Because the cathode is cooled by electron extraction and radiation, cathode heat losses only represent between 5 and 10% of measured total losses. The heat losses are decomposed into Q_{elec}, including cathode and anode phenomena (particularly voltage falls, work functions of materials) Q_c and Q_r for heat transfer to

the anode wall by convection and radiation, respectively. Thus,

$$Q_{\text{loss}} = Q_{\text{elec}} + Q_{\text{c}} + Q_{\text{r}} \tag{5}$$

The radiative losses Q_{r} can be estimated by using the effective volumetric emission coefficient of a nitrogen plasma taking into account self-absorption [18]. If a nitrogen plasma at 10^4 K uniformly fills the entire volume of the nozzle channel (1.6×10^{-7} m^3), then approximately 40 W escape by radiation to the anode wall.

The order of magnitude of the conductive heat flux to the wall, Q_{c}, is estimated by using the heat potential $\varphi(T) = \int K(T')\mathrm{d}T'$ where K is the thermal conductivity of nitrogen plasma that takes into account the translational and reactive thermal conductivities [18, 26]. φ presents a smooth evolution with the specific enthalpy, h, and can be accurately evaluated following $\varphi(h) = ah^2 + bh + c$, where a, b, and c are known constants [28]. By doing so, it is possible to take into account the dissociation–recombination process that makes nitrogen very efficient for heat transfer. Qualitatively, the energy that is absorbed in one place for dissociation is released in another place with molecular recombination, efficiently participating in heat conduction.

Neglecting the axial development of the arc jet, the heat flux to the nozzle wall is obtained by:

$$Q_{\text{c}} = -\pi DL\left[\left(\frac{\mathrm{d}\varphi}{\mathrm{d}h}\right)\left(\frac{\mathrm{d}h}{\mathrm{d}r}\right)\right]_{\text{D/2}} \tag{6}$$

using equation (3) and using $h_{\text{L}} = \bar{h}_{\text{L}}$ for the steady state yields:

$$Q_{\text{c}} = 8\pi(2ah_{\text{w}} + b)L(\bar{h}_{\text{L}} - h_{\text{w}}) \tag{7}$$

Because $h_{\text{w}} \ll \bar{h}_{\text{L}}$ ($h_{\text{w}} \sim 0.2$ MJ kg^{-1} for a wall temperature of approximately 500 K), equation (7) is simplified:

$$Q_{\text{c}} \approx \alpha_{\text{c}} L \bar{h}_{\text{L}} \tag{8}$$

where $\alpha_{\text{c}} = 8\pi(2ah_{\text{w}} + b) = 1.88 \times 10^{-3}$ kg m^{-1}s^{-1}.

The evaluation of convective losses Q_{c} for $L = 13$ mm and time and space averaged specific enthalpy $\bar{h}_{\text{L}} = 13.4$ MJ kg^{-1} yields approximately 330 W. Consequently, the radiative heat losses Q_{r} are much smaller than convective heat losses Q_{c}, so that the linear relationship between heat losses and enthalpy is considered as valid in the following. However, the proportionality constant between the heat losses and enthalpy is experimentally determined and is noted α_{cr} because it takes implicitly into account both radiation and thermal conduction.

Introducing $V_{\text{elec}} = Q_{\text{elec}}/I$, which is supposed to be constant, the stationary heat balance of the torch is rewritten as

$$\bar{V} - \frac{q_{\text{m}}\bar{h}_{\text{L}}}{I} = V_{\text{elec}} + \alpha_{\text{cr}}\frac{L\bar{h}_{\text{L}}}{I} \tag{9}$$

where the quantities $V^* = \bar{V} - \frac{q_{\text{m}}\bar{h}_{\text{L}}}{I}$ and $X^* = \frac{L\bar{h}_{\text{L}}}{I}$ can be measured so that equation (9) becomes $V^* = V_{\text{elec}} + \alpha_{\text{cr}}X^*$ and can be tested experimentally by changing the channel length, L, and performing calorimetric investigations as mentioned above. Figure 12 shows the dependence of V^* on X^* for different sets of experimental parameters. The linear dependence is satisfactorily highlighted and the slope yields $\alpha_{\text{cr}} = 1.01 \pm 0.3\ 10^{-3}$ kg m^{-1} s^{-1}, which remains smaller than the theoretical value of 1.88 10^{-3} kg m^{-1} s^{-1}. The latter is overestimated because it does not take into account the axial development of the arc into the nozzle channel. The voltage decline due to electrode phenomena is $V_{\text{elec}} = 17.4 \pm 4.0$ V.

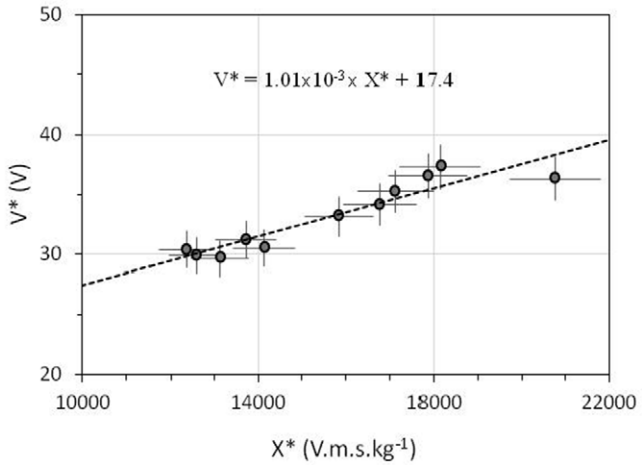

Figure 12. Heat balance expressed in terms of V^* on X^* for different sets of experimental parameters (see equation (9)).

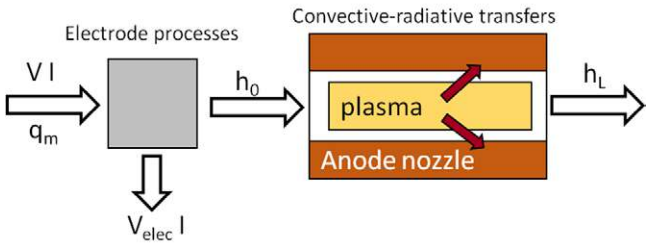

Figure 13. Scheme of the simplified analytic model of heat transfer inside the anode nozzle in transient regime. q_{m} is the mass flow rate, V is the torch voltage, and I is the electric current.

4.3. Heat transfers in transient regime

In the following, a simplified approach of heat transfer mechanisms in transient regime is developed to estimate the influence of arc voltage fluctuations on enthalpy variations. The mechanisms responsible for heat losses due to electrode phenomena (i.e. V_{elec}) are assumed to be decoupled from those responsible for convection and radiative heat transfers. The experimental values of $\alpha_{\text{cr}} = 1.01 \times 10^{-3}$ kg m^{-1} s^{-1} and $V_{\text{elec}} = 17.4$ V are used in the transient regime.

Figure 13 represents the basic scheme of such a simplified approach where the processes responsible for Q_{elec} and ($Q_{\text{c}} + Q_{\text{r}}$) are decoupled.

The specific enthalpy, h_0, that should be available in the absence of conductive and radiative heat transfer to the nozzle wall, is given by:

$$q_{\text{m}}h_0 = (V - V_{\text{elec}})\, I \tag{10}$$

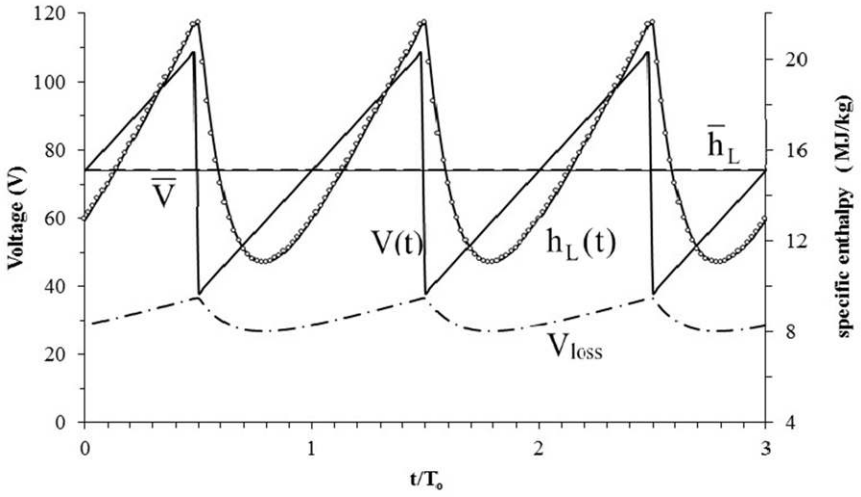

Figure 14. Theoretical evolutions of arc voltage $V(t)$ (solid line, left scale), and specific enthalpy at the nozzle exit, $h_L(t)$ (open circle, right scale). $T_0 = 710\,\mu$s. The horizontal line shows both voltage and enthalpy mean value. V_{loss} is an equivalent voltage that represents heat losses at 15 A.

By using quantities averaged over the channel cross-section, $S = \pi D^2/4$, the 1D energy conservation equation in a fluid and applied to the plasma in the nozzle is written as:

$$\rho\frac{\partial h}{\partial t} + \rho u\frac{\partial h}{\partial z} = -p_{th} \tag{11}$$

z is the axial coordinate, with $0 < z < L$, ρ and u are, respectively, the mass density and plasma velocity, and p_{th} is the power per unit volume lost by heat transfer to the anode, so that $p_{th}SL = \alpha_{cr}Lh_L$. The input enthalpy $h(z = 0) = h_0$ is given by equation (10).

The variables in equations (10) and (11) comprise a time-averaged component (bar notation) and a fluctuating component (prime notation), so that: $h_L = \bar{h}_L + h'$, $h_0 = \bar{h}_0 + h'_0$, and $V = \bar{V} + v'$. The mass flow rate, $q_m = \rho$uS, is supposed to be constant and the fluctuant component of specific enthalpy is supposed to be independent of z. Following these simplifications, equation (11) is linearized, integrated over z from 0 to L, and time-averaged variables are separated from fluctuant ones. Then:

$$\bar{h}_L = \frac{(\bar{V} - V_{elec})}{q_m + \alpha_{cr}L}I \tag{12}$$

$$\rho LS\frac{dh'}{dt} + q_m(h' - h'_0) = -\alpha_{cr}Lh' \tag{13}$$

Note that in equation (12) the heat loss term, $\alpha_{cr}L$, is equivalent to a mass flow rate that reduces the available specific enthalpy at the torch exit. Taking into account that $q_m h_0' = v'I$, equation (13) can be rewritten as follows by using (10):

$$\frac{dh'}{dt} + \frac{h'}{\tau_0} = \frac{I}{(q_m + \alpha_{cr}L)}\frac{v'}{\tau_0} \tag{14}$$

where τ_0 is a characteristic time checking $\frac{1}{\tau_0} = \frac{1}{\tau_{res}} + \frac{1}{\tau_{tr}}$. The residence time τ_{res} and the characteristic time of heat transfer τ_{tr} are given by:

$$\tau_{res} = \frac{L}{u} = \frac{m_p}{q_m} \text{ and } \tau_{tr} = \frac{m_p}{\alpha_{cr}L} \tag{15}$$

where the mass of plasma contained in the nozzle channel is $m_p = \rho$SL. ρ is evaluated as a function of $\bar{h}_L$ following thermodynamic data. This yields $m_p = 7.6\ 10^{-9}$ kg.

Equation (14) shows that the fluctuant components of enthalpy and arc voltage obey a first-order ordinary differential equation in which the residence time of the plasma in the nozzle together with heat transfer play an important role through the characteristic time τ_0.

For experimental conditions described in section 2.1, it is found that $\tau_{res} = 170\ \mu$s, $\tau_{tr} = 588\ \mu$s, and $\tau_0 = 132\ \mu$s.

The problem is solved by using a Fourier's series expansion and the solution $h_L(t)$ is given in the appendix.

Figure 14 depicts the time-dependence of space-averaged specific enthalpy at the nozzle exit, $h_L(t)$. An equivalent voltage, $V_{loss} = Q_{loss}/I$, is reported in figure 14 as $V_{loss}(t) = V_{elec} + \alpha_{cr}Lh_L(t)/I$ and can be directly compared to the torch voltage $V(t)$. It must be underlined that Q_{loss} cannot be assessed by time-resolved measurements because of the thermal inertia of cooling circuits. The mean values of V_{loss} and $\bar{h}_L$ given by the model are 32 V and 15.0 MJ kg^{-1}, respectively, instead of 36 V and 13.7 MJ kg^{-1} for the measurements.

Following the simplified model that the specific enthalpy oscillates between approximately 11 and 21.5 MJ kg^{-1}, this interval is compatible with the values obtained by OES, $h_L^{min} = 9.5 \pm 1.5$ and $h_L^{max} = 25.5 \pm 1.5$ MJ kg^{-1} shown in figure 11. The shape of the signal $h_L(t)$ is smoothed compared to $V(t)$ thanks to the low pass filtering effect due to the presence of τ_0 in equation (14). If τ_0 had been 0, then the enthalpy and voltage modulation ratios would have been the same, i.e. 17.

It can be noted that the maxima of enthalpy are almost synchronous with the maxima of arc voltage, whereas the minima of enthalpy exhibit a time lag of approximately 230 μs, approximately one-third of the period, with respect to the minima of arc voltage. This time delay accounts for the dynamics of heat

Table 1. Comparison of the measurements of rotational temperature and weighted temperature following the results of figure 9.

$V(t)$ (V)	$h_L(t)$ MJ kg^{-1}	$\bar{T}(h_L)$ (K)	T_{rot} (K)
62 +/− 1.5	11	6400	6280 +/− 250
75 +/− 1.5	13 +/− 0.4	6700 +/− 50	6460 +/− 250
85 +/− 1.5	15 +/− 0.4	6900 +/− 50	6600 +/− 250
105 +/− 1.5	21	7400	7540 +/− 150

transfer from plasma to the anode nozzle, which depends on the characteristic time, $\tau_{tr,}$ for heat conduction and on residence time, τ_{res}, of the plasma in the channel. τ_0 appears as a relaxation time that is a combination of τ_{res} and τ_{tr} following Matthiessen's rule. In figure 14 the decreasing branches of $h_L(t)$ are related to an extinguishing plasma, created during the previous period of voltage, instead of the raising branches that correspond to an energy amount that grows following the voltage increase of the actual period. In figure 5(a), the time delay corresponds to the end of one of those decreasing branches and figure 5(b) corresponds to the beginning of the raising branch. Both of those pictures correspond to a specific enthalpy close to its minimum. Due to the time delay in figure 5(c), the voltage is close to its mean value, but the specific enthalpy is approximately 2 MJ kg^{-1} below its own mean value, following figure 14.

The minimum enthalpy, h_L^{min}, defined in figure 11 and that was thought as a threshold value under which OES cannot detect sufficient reliable spectrum, is in reality a true minimum. That means there is no weighted temperature $\bar{T}(h_L)$ below approximately 6000 K. The experimental results presented in figure 9 are interpreted thanks to the model that gives the link between the instantaneous voltage $V(t)$ and the specific enthalpy at the nozzle exit $h_L(t)$ (figure 14) and, then, following the link between $h_L(t)$ and the weighted temperature, $\bar{T}(h_L)$ (equation 4). The results given in table 1 show a reasonable agreement between the measured temperature, T_{rot}, and the predicted value of $\bar{T}(h_L)$, although the model of section 4.3 is rather simple and the constant α_{cr} and V_{elec} that are involved are of weak precision.

However, the use of the model together with the notion of weighted temperature is of considerable help for the interpretation of the temperature measurements, especially for understanding the timing between instantaneous voltage, which is easily measurable, and the instantaneous specific enthalpy available at the nozzle exit, which is only accessible by optical means.

5. Conclusion

Finely structured ceramic coatings with intermediate thicknesses (2–20 μm) can be manufactured by plasma spraying techniques. A liquid phase as carrier medium must be used to give enough momentum to nanosized solid particles to be injected in the plasma core. They can also be directly synthesized in-flight after vaporization of solution precursors and subsequently sprayed onto substrates. The interaction dynamics between plasma and materials depends on plasma stability or on the process ability to reproduce in time the same heat and momentum exchanges. Most current studies are devoted to limit the arc motion inside the plasma torch to improve the stability process.

Instead, in this chapter, it is proposed to favour the arc motion to obtain a self-sustained pulsed jet. The resulting nitrogen arc jet produces a time-modulation of enthalpy at the nozzle exit that can be used to control the heat and momentum transfers by adjusting the injection timing of materials. Measurements of rotational temperatures obtained by time-resolved optical emission spectroscopy have shown that they change in the temperature range of 6000 to 8000 K. Due to the dissociation of the nitrogen molecule, heat transfers are particularly efficient and can be described in terms of heat conduction potential, which is directly dependent on the specific enthalpy of plasma. In the experimental conditions presented, the modulation of enthalpy (h_L^{max}/h_L^{min}) at the nozzle exit was shown to be close to 2.68. This modulation ratio was checked by a simplified model of the dynamics of heat transfer inside the torch nozzle, which has confirmed the spectroscopic measurements. The model has permitted interpretation of time-resolved measurements and has especially highlighted a time delay between the arc voltage and the enthalpy at the nozzle exit. This delay accounts for the characteristic time of heat transfers and the residence time of plasma inside the nozzle. It results in a low-pass filter effect on enthalpy that smoothes the fast variations of arc voltage.

Departure between the measured and calculated enthalpy modulation ratio can be explained by the simplified assumption of a constant mass flow rate in the model. An amplification effect of enthalpy should occur when the arc voltage and the gas flow rate are out of phase ($h_L \propto V/q_m$). This will be considered in a further chapter. Finally, the modulation of enthalpy suggests that plasma velocity is also time-dependent. Consequently, in further experiments of synchronous injection of materials in pulsed arc jet, this time-delay must be considered not only for heat transfers but also to control material trajectories that should then be reproducible. This study can be applied to conventional plasma torches used for plasma spraying for which oscillations following the Helmholtz mode have been reported. Most of these torches have voltage fluctuations of approximately 70 V peak-to-peak and with frequencies of approximately 4.5 kHz [14]. The specific enthalpies are comparable with those obtained in the present work (~15 MJ kg^{-1}).

Acknowledgments

The French National Research Agency is acknowledged for financial support in the frame of the PLASMAT program (ANR-12-JCJC-JS09-0006-01).

Appendix

Let $H(\omega)$ and $V(\omega)$ be the Fourier component of $h'(t)$ and $v'(t)$, respectively. Equation (14) can be changed into the following transfer function:

$$\frac{H(\omega)}{V(\omega)} = \left(\frac{I}{q_m + \alpha_{cr} L}\right) \frac{1}{1 + j\omega\tau_0} \tag{A.1}$$

Due to the shape of the voltage signal as seen in figure 2(b), $V(t)$ is approximated by a periodic function, T_0 in period,

$$V(t) = \bar{V} + \bar{A}\frac{t}{T_0}, \; -\frac{T_0}{2} < t < \frac{T_0}{2} \text{ and } V(t + T_0) = V(t) \tag{A.2}$$

where $\bar{V} = 75\,\text{V}$, $T_0 = 710\,\mu\text{s}$ and $\bar{A} = 70\,\text{V}$ are, respectively, mean voltage, the period of voltage signal, and its mean amplitude peak-to-peak shown in figure 2(b). Then, by using the Fourier expansions, $V(t)$ and $h_L(t)$ become:

$$V(t) = \bar{V} + \frac{\bar{A}}{\pi} \sum_{n=1}^{\infty} \frac{(-1)^{n+1}}{n} \sin(\omega_n t) \text{ with } \omega_n = n\frac{2\pi}{T_0} \tag{A.3}$$

$$h_L(t) = \overline{h_L} + \sum_{n=1}^{\infty} H_n \sin(\omega_n(t - \theta_n)) \tag{A.4}$$

$$\text{with } H_n = \frac{(-1)^{n+1}}{n\pi(q_m + \alpha_{cr} L)} \frac{\overline{A}\, I}{\sqrt{1 + (\omega_n \tau_0)^2}} \text{ and}$$

$$\theta_n = \frac{T_0}{2\pi n} \arctan(\omega_n \tau_0) \tag{A.5}$$

References

[1] Vardelle A, Moreau C, Themelis N J and Chazelas C 2015 *Plasma Chem. Plasma Process.* **35** 491–509
[2] Fauchais P, Rat V, Delbos C, Coudert J F, Chartier T and Bianchi L 2005 *IEEE Trans. Plasma Sci.* **33** 920–30
[3] Chen D, Jordan E H and Gell M 2010 *Plasma Chem. Plasma Process.* **30** 111–9
[4] Killinger A, Gadow R, Mauer G, Guignard A, Vaßen R and Stöver D 2011 *J. Therm. Spray Technol.* **20** 677–695
[5] Meillot E, Vincent S, Caruyer C, Damiani D and Caltagirone J P 2013 *J. Phys. D: Appl. Phys.* **46** 224017
[6] Wutzke S A, Pfender E and Eckert E R G 1967 *AIAA J.* **5** 707–14
[7] Coudert J F, Planche M P and Fauchais P 1996 *Plasma Chem. Plasma Process.* **16** 211s–27s
[8] Ghorui S and Das A K 2004 *Phys. Rev.* E **69** 026408
[9] Trelles J P, Pfender E and Heberlein J V R 2007 *J. Phys. D: Appl. Phys.* **40** 5635–48
[10] Coudert J F, Rat V and Rigot D 2007 *J. Phys. D: Appl. Phys.* **40** 7357–66
[11] Huang H, Pan W and Wu C 2012 *Plasma Chem. Plasma Process.* **32** 65–74
[12] Krowka J, Rat V and Coudert J F 2013 *J. Phys. D: Appl. Phys.* **46** 505206
[13] Nemchinsky V 2014 *IEEE Trans. Plasma Sci.* **42** 4026–30
[14] Rat V and Coudert J F 2010 *J. Appl. Phys.* **108** 043304
[15] Rat V and Coudert J F 2010 *Appl. Phys. Lett.* **96** 101503
[16] Schein J, Zierhut J, Dzulko M, Forster G and Landes K D 2007 *Contrib. Plasma Phys.* **47** 498–504
[17] Krowka J, Rat V and Coudert J F 2013 *J. Phys. D: Appl. Phys.* **46** 224018
[18] Boulos M I, Fauchais P and Pfender E 1994 *Thermal Plasmas* vol 1 (New York and London: Plenum)
[19] De Vos J C 1954 *Physica* **20** 690–714
[20] Herzberg G 1950 *Molecular Spectra and Molecular Structure* (Princeton, NJ: van Nostrand-Reinhold)
[21] Laux C O, Spence T G, Kruger C H and Zare R N 2003 *Plasma Sources Sci. Technol.* **12** 125–38
[22] Laux C O, Gessman R J, Kruger C H, Roux F, Michaud F and Davis S P 2001 *J. Quant. Spectrosc. Radiat. Transf.* **68** 473–82
[23] Nassar H, Pellerin S, Musiol K, Martinie O, Pellerin N and Cormier J M 2004 *J. Phys. D: Appl. Phys.* **37** 1904–16
[24] Laux C O 2002 Radiation and nonequilibrium collisional-radiatvie models (von Karman Institute Special Course on Physico-chemical Modeling of High Enthalpy and Plasma Flows Rhode-Saint-Genèse, Belgium 4–7 June 2002)
[25] Bruggeman P J, Sadeghi N, Schram DC and Linss V 2014 *Plasma Sources Sci. Technol.* **23** 23001
[26] Pateyron B, Delluc G 1986 Software TTWinner, ADEP—Banque de données de l'Université et du CNRS Ed. Direction des Bibliothèques, des Musées et de l'Information Scientifique et technique http://ttwinner.free.fr
[27] Tanaka Y, Nagumo T, Sakai H, Uesugi Y, Sakai Y and Nakamura K 2010 *J. Phys. D: Appl. Phys.* **43** 265201
[28] Rat V and Coudert J F 2006 *J. Phys. D: Appl. Phys.* **39** 4799–807